LETTER

https://doi.org/10.1038/s41586-018-0188-x

Velocity-resolved kinetics of site-specific carbon monoxide oxidation on platinum surfaces

Jannis Neugebohren[1], Dmitriy Borodin[1], Hinrich W. Hahn[1], Jan Altschäffel[1,2], Alexander Kandratsenka[2], Daniel J. Auerbach[2], Charles T. Campbell[3], Dirk Schwarzer[2], Dan J. Harding[1,2,7], Alec M. Wodtke[1,2,4] & Theofanis N. Kitsopoulos[2,5,6]*

Catalysts are widely used to increase reaction rates. They function by stabilizing the transition state of the reaction at their active site, where the atomic arrangement ensures favourable interactions[1]. However, mechanistic understanding is often limited when catalysts possess multiple active sites—such as sites associated with either the step edges or the close-packed terraces of inorganic nanoparticles[2–4]—with distinct activities that cannot be measured simultaneously. An example is the oxidation of carbon monoxide over platinum surfaces, one of the oldest and best studied heterogeneous reactions. In 1824, this reaction was recognized to be crucial for the function of the Davy safety lamp, and today it is used to optimize combustion, hydrogen production and fuel-cell operation[5,6]. The carbon dioxide products are formed in a bimodal kinetic energy distribution[7–13]; however, despite extensive study[5], it remains unclear whether this reflects the involvement of more than one reaction mechanism occurring at multiple active sites[12,13]. Here we show that the reaction rates at different active sites can be measured simultaneously, using molecular beams to controllably introduce reactants and slice ion imaging[14,15] to map the velocity vectors of the product molecules, which reflect the symmetry and the orientation of the active site[16]. We use this velocity-resolved kinetics approach to map the oxidation rates of carbon monoxide at step edges and terrace sites on platinum surfaces, and find that the reaction proceeds through two distinct channels[11–13]: it is dominated at low temperatures by the more active step sites, and at high temperatures by the more abundant terrace sites. We expect our approach to be applicable to a wide range of heterogeneous reactions and to provide improved mechanistic understanding of the contribution of different active sites, which should be useful in the design of improved catalysts.

The oxidation of CO on the (111) surface of platinum—the simplest close-packed single-crystal surface—proceeds through the Langmuir–Hinshelwood mechanism[7,17]. O_2 is activated by dissociating into adsorbed oxygen atoms, which combine with adsorbed CO to form CO_2 with substantial excess energy. This can lead to hyperthermal CO_2, which has high kinetic and internal energy[8,9] and exhibits angular distributions that are narrower than those expected for a molecule at thermal equilibrium with the surface[7,9,10]; however, some reaction conditions also result in a thermal channel[11–13]. Although this bimodal generation of products suggests that CO oxidation occurs through more than one reaction[12,13], the dominant view at present is that all products form through the same transition state, and a fraction desorbs promptly with hyperthermal velocities whereas the rest become trapped and thermalized at the surface before desorbing[11].

Our study of this reaction exploits the correlation between the angle and velocity of reaction products and the symmetry and orientation of surface reaction sites[16]. This enabled us to extract site-specific kinetic data by data-mapping the temporal evolution of velocity-resolved products. We used pulsed-molecular-beam surface dosing of both CO and O_2 in combination with slice ion imaging[14,15]. The O_2 beam was used to control oxygen coverage and the pulsed CO beam was used to initiate the reaction; together with synchronized pulsed-laser ionization of CO_2, this enabled us to obtain the CO_2 flux as a function of reaction time. At each time point in the reaction, ion imaging provided distributions of the velocity vectors of the products.

For CO oxidation on Pt(111) with a step density of 0.25%, ion images of the CO_2 produced (Fig. 1a) show a bimodal speed distribution[12,13] (Fig. 1b). The low-velocity component was fit to a Maxwell–Boltzmann distribution, whereas the high-velocity component is hyperthermal. The angular distributions of the two channels (Fig. 1c) show that the hyperthermal component has a sharp peak along the surface normal (approximately $\cos^8\theta$), whereas the thermal channel follows a $\cos\theta$ distribution.

To obtain site-specific kinetics, we recorded the integral of the ion image intensity over selected velocity ranges (red and blue rectangles in the inset of Fig. 2) as a function of the delay between the CO and laser pulses. The raw time-dependent signals are proportional to product density and depend not only on the reaction time at the surface, but also on the flight time of the CO_2 from the surface to the ionizing laser spot. By recording the velocity of the products (see Methods), we corrected for the CO_2 flight-time and obtained the relative flux in both channels. From the measured angular distributions, we corrected the signal strength to reflect the true branching ratio between the two channels. Thus, we rigorously obtained the relative product flux as a function of reaction time, hereafter referred to as the kinetic trace.

Kinetic traces are shown in Fig. 2 for both the hyperthermal (red) and thermal (blue) channels. In both, the CO_2 formation rate first increases as CO adsorbs onto the surface (black dashed line), and then decays with an effective lifetime, τ_{eff} (see Methods), as the adsorbed CO is removed. τ_{eff} for the thermal and hyperthermal channels—hereafter referred to as $\tau_{\mathrm{eff}}^{\mathrm{Step}}$ and $\tau_{\mathrm{eff}}^{\mathrm{Terr}}$, respectively—are quite different; $\tau_{\mathrm{eff}}^{\mathrm{Terr}}$ is shorter than $\tau_{\mathrm{eff}}^{\mathrm{Step}}$ under all conditions in this study. This is inconsistent with a bimodal velocity distribution resulting from partial thermalization of products from a single reaction[7,11], as that would require the two kinetic traces to be identical. It should be noted that the desorption of physisorbed CO_2 is fast compared to the reaction time.

We assign the hyperthermal and thermal channels to the reaction of CO with oxygen adatoms at terraces and steps, respectively, for three reasons. First, when we increased the step density 66-fold using a Pt(332) crystal, the hyperthermal channel disappeared completely at low oxygen coverage, at which nearly all oxygen atoms are bound at steps (lower left inset of Fig. 2). This confirms that the hyperthermal channel does not occur at steps. Second, in the limit of zero oxygen coverage, τ_{eff} is determined by any non-reactive channels that consume adsorbed CO (see Methods). For the thermal channel, the zero-coverage rate constants (filled blue circles in Extended Data Fig. 4) are in excellent agreement with known values of CO desorption from steps[18], confirming that CO molecules adsorbed at steps (hereafter

[1]Institute for Physical Chemistry, University of Goettingen, Göttingen, Germany. [2]Department of Dynamics at Surfaces, Max Planck Institute for Biophysical Chemistry, Göttingen, Germany. [3]Department of Chemistry, University of Washington, Seattle, WA, USA. [4]International Center for Advanced Studies of Energy Conversion, Georg-August University of Göttingen, Göttingen, Germany. [5]Department of Chemistry, University of Crete, Heraklion, Greece. [6]Institute of Electronic Structure and Laser, FORTH, Heraklion, Greece. [7]Present address: Department of Chemical Engineering, KTH Royal Institute of Technology, Stockholm, Sweden. *e-mail: tkitsop@mpibpc.mpg.de

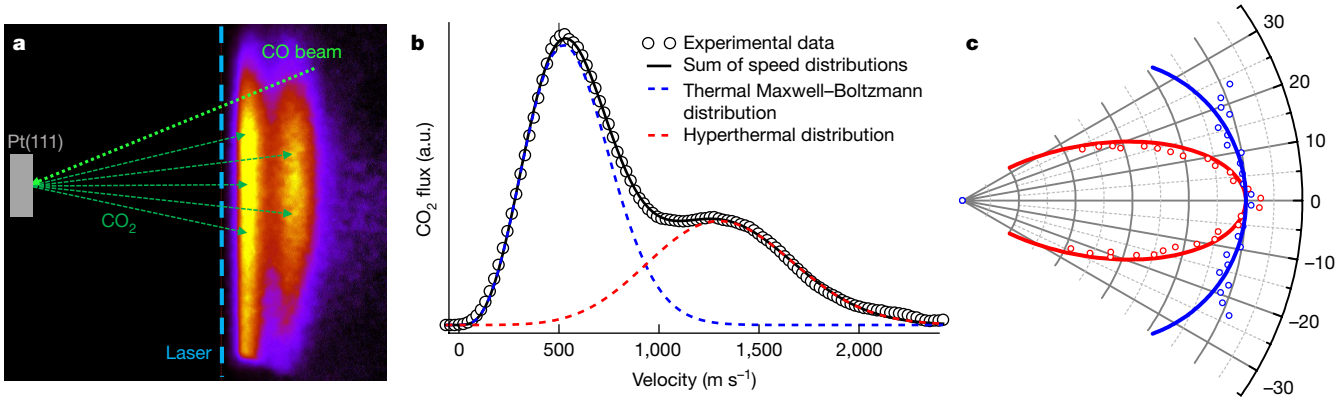

Fig. 1 | Slice ion imaging of CO_2 produced by CO oxidation at Pt(111). **a**, Ion image of CO_2 produced by the catalytic oxidation of CO on a Pt(111) surface. The velocity vector of the incident CO beam is shown by the light green arrow, as are a few of the CO_2 product vectors appearing in the thermal and hyperthermal channels. CO_2 speed increases to the right. The position of the ionizing laser beam is shown by the dashed blue line. **b**, Velocity probability distribution of CO_2 molecules. The thermal product channel is fitted to a Maxwell–Boltzmann function (translational temperature, $T_{trans} = 483$ K; dashed blue line) and the hyperthermal channel is fit to a flowing Maxwell–Boltzmann function ($T_{trans} = 894$ K, $\alpha = 190$ meV; dashed red line). **c**, Velocity-resolved angular distributions: hyperthermal (red) and thermal (blue) channels. The hyperthermal channel is compared to a $\cos^8\theta$ function (red line) and the thermal channel is compared to a $\cos\theta$ function (blue line). a.u., arbitrary units.

denoted CO_a^{Step}) are important to the thermal reaction. Third, we calculated the minimum energy path of the terrace reaction $CO_a^{Terr} + O_a^{Terr}$ using density functional theory (DFT; see Methods). This shows an energy release of 1.9 eV and an early transition-state structure (that is, it resembles the reactants), which is consistent with the average translational energy release of 0.38 eV that is seen in the hyperthermal channel. This assignment is also consistent with the previously observed dominance of the hyperthermal channel at 880 K[8] (see Methods) and the prevalence of the thermal channel that is seen with increased step density[11].

Considering the above, we interpret the kinetic traces of Fig. 2 in terms of competing reactions that occur with oxygen bound at terrace and step sites. We consider the terrace reaction competing with a process involving diffusion that converts CO_a^{Terr} to CO_a^{Step}. This explains how adsorption at terraces (more than 99% of the CO adsorbs initially at terraces, as the Pt(111) step density is less than 1%) can lead to more CO_2 production at steps. The kinetic trace of the thermal channel shown in Fig. 2 cannot be fit with a single exponential function (see Extended Data Figs. 6, 8), which suggests the presence of two step reactions.

In Methods, we present a simple kinetic model that describes our data over the full range of oxygen coverages and surface temperatures using three reactions:

$$CO_a^{Terr} + O_a^{Terr} \xrightarrow{k_2^{TT}} CO_2^{hyperthermal}$$

$$CO_a^{Terr} + O_a^{Step} \xrightarrow{k_2^{TS}} CO_2^{thermal}$$

$$CO_a^{Step} + O_a^{Step} \xrightarrow{k_2^{SS}} CO_2^{thermal}$$

We also include CO_a^{Step} desorption, as well as CO_a^{Terr} desorption and conversion of CO_a^{Terr} to CO_a^{Step}. The determination of oxygen coverage and the O_a^{Step}:O_a^{Terr} ratio is described in Methods. We note that velocity-resolved kinetics of CO oxidation on Pt(332), where the step density is 66-fold higher, supports the three-reaction mechanism.

The derived pre-exponential factors and activation energies are shown in Table 1 and the temperature dependent reaction rate constants are shown in Fig. 3. The results obtained on the Pt(111) and the Pt(332) crystals agree well. The rate constants for CO oxidation at steps are similar to those for reaction at terraces. Despite this, the product yield through step reactions dominates at all temperatures used in this work and in previous studies (area to the left of the vertical line in Fig. 3). Even for a Pt(111) crystal with a step density of only 0.25%, reactions at steps dominate. Analysis with our kinetic model shows that this reflects the fact that conversion of CO_a^{Terr} to CO_a^{Step} is much faster than the TT reaction in the temperature range of this and previous work. We therefore conclude that all previous kinetics studies were strongly influenced by step reactions (see Methods).

For this reason, this is the first report to our knowledge of the rate parameters for the Pt(111) terrace reaction, k_2^{TT}. Only the rate of the TT reaction has been calculated from first principles[19,20]; as such, the new rate parameters provide the first opportunity to benchmark the ab

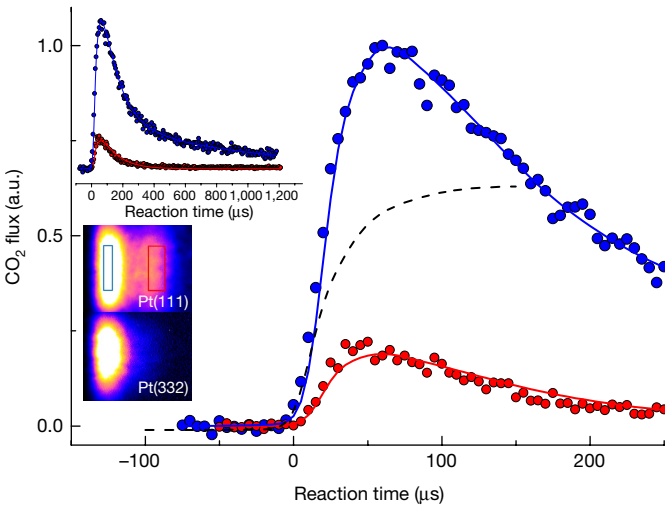

Fig. 2 | Kinetic traces of CO_2 obtained from velocity-resolved kinetics experiments. The inset labelled Pt(111) shows an ion image with velocity-space integration windows for the hyperthermal (red; 1,280–1,610 m s^{-1}) and the thermal (blue; 420–590 m s^{-1}) channels. The dashed black line represents the measured CO dosing function; the onset of the incident CO beam is taken as the zero of time. The solid red and blue lines are the fits resulting from the kinetic model (see Methods). The two traces are normalized to reflect the experimental time-integrated branching ratio between the two channels (8.6:1 in favour of the thermal channel) at this temperature and oxygen coverage. The step density was 0.0025 monolayers, the oxygen coverage was 0.04 monolayers and the dose of a single CO pulse was 2×10^{-5} monolayers. The surface temperature was 593 K. The experimental conditions for the (332) image are: oxygen coverage, 0.04 monolayers; surface temperature, 593 K; step density, 0.167 monolayers. Here, oxygen atoms are expected to be entirely at step sites, because O_2 dissociates more easily at steps than at terraces[29] and oxygen atoms are bound more strongly at steps than at terraces[30]. For the reaction on the (332) sample, the hyperthermal channel is absent.

Table 1 | Rate parameters for the elementary processes involved in the site-specific oxidation of carbon monoxide on a platinum catalyst

	Elementary process	A (s^{-1})	E_a (eV)
k_0^T	Desorption from terraces[a]	$5.9^{+5.4}_{-2.8} \times 10^{13}$	1.28 ± 0.02
k_0^S	Desorption from steps[b]	$1.5^{+2.5}_{-0.6} \times 10^{12}$	1.18 ± 0.056
k_1^{TS} 111 (332)	Diffusion from terrace to step[c]	$2.1^{+13}_{-1.8} \times 10^6$ (1.5×10^6)	0.30 ± 0.1 (0.32 ± 0.1)
k_2^{TT} 111 (332)	$CO_{Terr} + O_{Terr}$ reaction	$3.5^{+21}_{-3.0} \times 10^9$ ($3.8^{+23}_{-3.3} \times 10^9$)	0.6 ± 0.1 (0.6 ± 0.1)
Theory[19]		$\mathbf{5.1 \times 10^{12}}$	**0.74**
k_2^{TS} 111 (332)	$CO_{Terr} + O_{Step}$ reaction	$5.9^{+36}_{-5.1} \times 10^7$ ($4.1^{+25}_{-3.5} \times 10^7$)	0.40 ± 0.1 (0.40 ± 0.1)
k_2^{SS} 111 (332)	$CO_{Step} + O_{Step}$ reaction	$2.9^{+18}_{-2.5} \times 10^9$ ($2.6^{+16}_{-2.2} \times 10^9$)	0.65 ± 0.1 (0.65 ± 0.1)

The rate parameters reported here should be used with caution outside the temperature range used in this work.
[a]Measured independently, as published in ref. [26]. This value also compares well with previous reports. See ref. [27]: $A = 3.5^{+7.2}_{-2.7} \times 10^{13}\,s^{-1}$, $E_a = 1.27 \pm 0.07$ eV.
[b]Obtained from measurements of desorption of CO from Pt(332). Compares well with rate constants reported in ref. [27].
[c]An activation energy of 0.3 eV was chosen following ref. [28]. This should be considered an effective conversion rate.

initio rates of this important catalytic reaction. Figure 3 shows one such calculation of the rate constants of the TT reaction, for which DFT is used to generate input for a transition-state-theory calculation of the rate constant[19]. The theoretical rate constant is 20–100 times larger than that seen experimentally. The theoretically calculated activation energy is higher than that derived from experiment (Table 1), as is expected when using a revised Perdew–Burke–Ernzerhof (RPBE) functional[21]. Improving the calculation would lower the barrier; however, this would only amplify the disagreement with experiment. Thus, it is clear that the theory fails to reproduce the prefactor of the rate constant. This can be the result of an incorrect treatment of reactant entropy[22] and/or dynamical recrossing at the transition state.

Velocity-resolved kinetics provides a powerful tool for catalytic kinetic studies. Previous studies have attempted to obtain CO oxidation kinetics without velocity resolution by measuring phase shifts with modulated reactant molecular beams[7,23]. To analyse these phase-lag data, the kinetic trace was assumed to follow a single exponential decay[7,23]; this was effectively a single-reaction assumption that resulted in an activation energy that was dependent on oxygen coverage[7]. However, we show in Methods that these were only apparent activation energies that result from the temperature and oxygen-coverage-dependent influence of the step and terrace reactions.

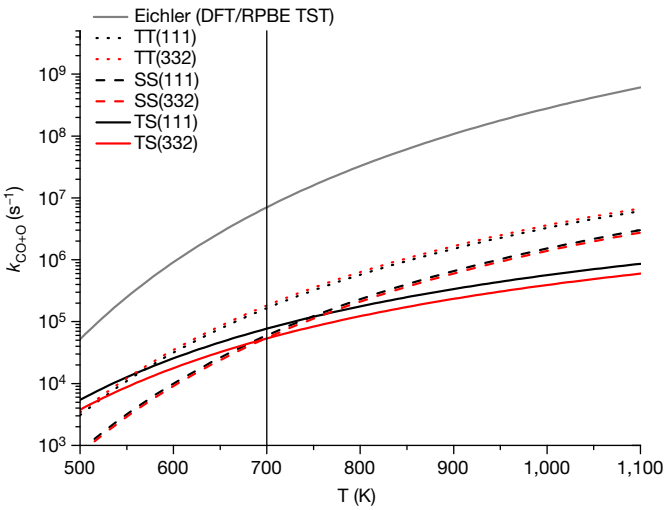

Fig. 3 | Rate constants for CO oxidation on platinum steps and terraces. Three reactions are identified in this work: the reaction of CO_a^{Terr} with terrace-bound oxygen atoms (TT) and two reactions of step-bound oxygen atoms with CO_a^{Steps} (SS) and CO_a^{Terr} (TS). Results obtained from a Pt(111) surface with a step density of 0.25% and those obtained from a Pt(332) crystal with a step density of 16.7% are shown as black and red lines, respectively. The units of the rate constant are those used when oxygen coverage is given as a (unitless) fraction of a monolayer. The grey line shows the results of transition-state theory (TST) calculations of the TT reaction rate based on a DFT calculation of the transition state[19]. It considerably overestimates reactivity. The region to the left of the vertical line shows the range of temperatures studied here and in previous studies. The region to the right of this line shows the range of temperatures typical for industrial catalysis.

The phase-lag method is analogous to frequency domain kinetic methods that are used in biophysics for obtaining (exponential) fluorescence lifetimes[24], and was the main method used before the advent of pulsed-laser-based pump–probe methods. In providing the kinetic trace directly, velocity-resolved kinetics serves the function of a pump–probe experiment for neutral matter. This enabled us to easily identify three elementary reactions that comprise a site-specific mechanism of CO oxidation on platinum. The activation energies for these three reactions are not dependent on oxygen coverage.

The relative importance of different reacting geometries occurring at different active sites has been described previously in terms of a geometry probability-weighted activation energy[25]: $E_{ai}^w = E_{ai} - kT\ln A_i$. Here A_i is the abundance of the ith reacting geometry and E_{ai} is its activation energy. The results of this work reveal that the values of A_i depend on diffusion and desorption, an outcome that is also relevant to real-world catalysts that are often operated at high temperatures. In Extended Data Fig. 10 we show that the terrace reaction dominates on Pt(111) and Pt(332) at high temperatures, whereas at low temperatures the step reactions dominate. At high temperature, CO desorption becomes much faster than CO diffusion; as such, the site of CO adsorption determines which reaction occurs. Because step edges are minority sites on both samples, adsorption (and therefore reaction) occurs primarily at terraces. Extended Data Fig. 10 also shows that, under high-temperature conditions in which CO desorption suppresses the importance of diffusion, the efficiency of the conversion from CO to CO_2 is also reduced. We suggest that this may be a general phenomenon: low-concentration, high-reactivity defects on surfaces will be important in low-temperature catalysis in which reactant diffusion is faster than desorption, whereas at high temperatures, the majority facet dominates the chemistry and the efficiency of the reaction decreases.

Online content

Any Methods, including any statements of data availability and Nature Research reporting summaries, along with any additional references and Source Data files, are available in the online version of the paper at https://doi.org/10.1038/s41586-018-0188-x.

Received: 21 September 2017; Accepted: 16 April 2018;
Published online 13 June 2018.

1. Garcia-Viloca, M., Gao, J., Karplus, M. & Truhlar, D. G. How enzymes work: analysis by modern rate theory and computer simulations. *Science* **303**, 186–195 (2004).
2. Mavrikakis, M., Stoltze, P. & Nørskov, J. K. Making gold less noble. *Catal. Lett.* **64**, 101–106 (2000).
3. Jaramillo, T. F. et al. Identification of active edge sites for electrochemical H_2 evolution from MoS_2 nanocatalysts. *Science* **317**, 100–102 (2007).
4. Van Santen, R. A. Complementary structure sensitive and insensitive catalytic relationships. *Acc. Chem. Res.* **42**, 57–66 (2009).

5. Santra, A. K. & Goodman, D. W. Catalytic oxidation of CO by platinum group metals: from ultrahigh vacuum to elevated pressures. *Electrochim. Acta* **47**, 3595–3609 (2002).
6. Park, E. D., Lee, D. & Lee, H. C. Recent progress in selective CO removal in a H_2-rich stream. *Catal. Today* **139**, 280–290 (2009).
7. Campbell, C. T., Ertl, G., Kuipers, H. & Segner, J. A molecular-beam study of the catalytic-oxidation of CO on a Pt(111) surface. *J. Chem. Phys.* **73**, 5862–5873 (1980).
8. Becker, C. A., Cowin, J. P., Wharton, L. & Auerbach, D. J. CO_2 product velocity distributions for CO oxidation on platinum. *J. Chem. Phys.* **67**, 3394 (1977).
9. Cao, G. Y., Moula, M. G., Ohno, Y. & Matsushima, T. Dynamics on individual reaction sites in steady-state carbon monoxide oxidation on stepped platinum(113). *J. Phys. Chem. B* **103**, 3235–3241 (1999).
10. Palmer, R. L. & Smith, J. N. J. Molecular beam study of CO oxidation on a (111) platinum surface. *J. Chem. Phys.* **60**, 1453 (1974).
11. Segner, J., Campbell, C. T., Doyen, G. & Ertl, G. Catalytic-oxidation of CO on Pt(111) - the influence of surface-defects and composition on the reaction dynamics. *Surf. Sci.* **138**, 505–523 (1984).
12. Poehlmann, E., Schmitt, M., Hoinkes, H. & Wilsch, H. Bimodal angular and velocity distributions of CO_2 desorbing after oxidation of CO on Pt(111). *Surf. Rev. Lett.* **2**, 741–758 (1995).
13. Allers, K. H., Pfnur, H., Feulner, P. & Menzel, D. Fast reaction-products from the oxidation of CO on Pt(111) - angular and velocity distributions of the CO_2 product molecules. *J. Chem. Phys.* **100**, 3985–3998 (1994).
14. Gebhardt, C. R., Rakitzis, T. P., Samartzis, P. C., Ladopoulos, V. & Kitsopoulos, T. N. Slice imaging: A new approach to ion imaging and velocity mapping. *Rev. Sci. Instrum.* **72**, 3848–3853 (2001).
15. Harding, D. J., Neugebohren, J., Auerbach, D. J., Kitsopoulos, T. N. & Wodtke, A. M. Using ion imaging to measure velocity distributions in surface scattering experiments. *J. Phys. Chem. A* **119**, 12255–12262 (2015).
16. Matsushima, T. Angle-resolved measurements of product desorption and reaction dynamics on individual sites. *Surf. Sci. Rep.* **52**, 1–62 (2003).
17. Langmuir, I. Chemical reactions at low pressures. *J. Am. Chem. Soc.* **37**, 1139–1167 (1915).
18. Campbell, C. T., Ertl, G., Kuipers, H. & Segner, J. A molecular-beam investigation of the interactions of CO with a Pt(111) surface. *Surf. Sci.* **107**, 207–219 (1981).
19. Eichler, A. CO oxidation on transition metal surfaces: reaction rates from first principles. *Surf. Sci.* **498**, 314–320 (2002).
20. Acharya, C. K. & Turner, C. H. CO oxidation with Pt(111) supported on pure and boron-doped carbon: A DFT investigation. *Surf. Sci.* **602**, 3595–3602 (2008).
21. Díaz, C. et al. Chemically accurate simulation of a prototypical surface reaction: H_2 dissociation on Cu(111). *Science* **326**, 832–834 (2009).
22. Jørgensen, M. & Gronbeck, H. Adsorbate entropies with complete potential energy sampling in microkinetic modeling. *J. Phys. Chem. C* **121**, 7199–7207 (2017).
23. Schwarz, J. A. & Madix, R. J. Modulated beam relaxation spectrometry - its application to study of heterogeneous kinetics. *Surf. Sci.* **46**, 317–341 (1974).
24. Ross, J. A. & Jameson, D. M. Time-resolved methods in biophysics. 8. Frequency domain fluorometry: applications to intrinsic protein fluorescence. *Photochem. Photobiol. Sci.* **7**, 1301–1312 (2008).
25. Nørskov, J. K. et al. The nature of the active site in heterogeneous metal catalysis. *Chem. Soc. Rev.* **37**, 2163–2171 (2008).
26. Harding, D. J. et al. Ion and velocity map imaging for surface dynamics and kinetics. *J. Chem. Phys.* **147**, 013939 (2017).
27. Golibrzuch, K. et al. CO desorption from a catalytic surface: elucidation of the role of steps by velocity-selected residence time measurements. *J. Am. Chem. Soc.* **137**, 1465–1475 (2015).
28. Seebauer, E. & Allen, C. E. Estimating surface diffusion coefficients. *Prog. Surf. Sci.* **49**, 265–330 (1995).
29. Badan, C. et al. Step-type selective oxidation of platinum surfaces. *J. Phys. Chem. C* **120**, 22927–22935 (2016).
30. Jinnouchi, R., Kodama, K. & Morimoto, Y. DFT calculations on H, OH and O adsorbate formations on Pt(111) and Pt(332) electrodes. *J. Electroanal. Chem.* **716**, 31–44 (2014).

Acknowledgements A.M.W. acknowledges support from the Alexander von Humboldt Foundation. We acknowledge support from Deutsche Forschungsgemeinschaft (DFG) and the Ministerium für Wissenschaft und Kultur (MWK) Niedersachsen, and the Volkswagenstiftung under grant INST 186/952-1. C.T.C. acknowledges the Göttingen Academy of Sciences and the US National Science Foundation (grant CHE-1665077) for support.

Reviewer information *Nature* thanks E. Hasselbrink and the other anonymous reviewer(s) for their contribution to the peer review of this work.

Author contributions J.N. and H.W.H. performed experiments with Pt(111), analysed the data and contributed to the writing of the paper. D.B. carried out experiments on Pt(332) and analysed the data. J.A. and A.K. carried out DFT calculations and performed ab initio molecular dynamics simulations. C.T.C. contributed to experimental methodology development and contributed useful arguments that led to the discovery of the reaction mechanism. D.J.A. contributed to discussions of the mechanism and to the writing of the paper. D.S. contributed to the discussion of the mechanism. D.J.H. helped build the instrument and took data. A.M.W. conceived the experiment and contributed to writing the paper. T.N.K. developed the use of slice ion imaging for reactive surface scattering, took data, developed data analysis tools and contributed to writing the manuscript.

Competing interests The authors declare no competing interests.

Additional information
Extended data is available for this paper at https://doi.org/10.1038/s41586-018-0188-x.
Reprints and permissions information is available at http://www.nature.com/reprints.
Correspondence and requests for materials should be addressed to T.N.K.
Publisher's note: Springer Nature remains neutral with regard to jurisdictional claims in published maps and institutional affiliations.

METHODS

Experimental methods. The instrument used in this work has been described recently for the measurements of desorption rates of CO from Pt(111) and Pd(111)[26]. A platinum crystal is first prepared by argon ion sputtering and annealing. The O_2 (normal incidence) and CO (20° from normal) pulsed molecular beams cross at the platinum surface at a selected repetition rate ratio (RRR).We used 7-bar backing pressure for the O_2 beam with a nozzle opening time of 70 μs. This gave an O_2 flux of 1.1×10^{11} molecules per pulse. A 5% mixture of CO in He at a total backing pressure of 7 bar and a nozzle opening time of 25 μs gave a CO flux of 2.2×10^{10} molecules per pulse. The diameter of both molecular beams at the surface was 3 mm. The O_2 beam was always fired at least 500 μs before the CO beam. The CO pulse initiates the reaction and is consumed before the next CO pulse arrives. A single CO pulse alters the oxygen coverage negligibly. CO_2 products were photoionized by a nine-photon non-resonant absorption process induced by the focused output (20 cm focal length lens) of a Coherent Astrella Ti:sapphire laser producing 1–5 mJ per pulse with a pulse duration of 100 fs at a wavelength of 800 nm. The ion camera system was time-gated at a controlled delay with respect to the ionizing laser pulse to restrict detection to $m/z = 44$ (CO_2^+). The laser ionization pulse was synchronized to the CO dosing pulse; the delay between these two pulses is used to analyse the kinetics of the reaction and at each delay, ion images are recorded using modified DaVis software (LaVision). Angular distributions are obtained by physically scanning the focal point of the ionizing laser beam back and forth in front of the reacting surface while accumulating the ion image. For kinetics measurements, the laser position was fixed and reaction products were detected close to the surface normal. The RRR value corresponds to a specific oxygen coverage, which is measured in a separate titration experiment in which the O_2 beam is suddenly turned off and the CO_2 signal is recorded until all oxygen is removed from the surface. This is calibrated by titration against an oxygen-saturated platinum surface. See Methods section 'Total oxygen coverage, $[O_a]$, from a titration experiment'.

Conversion of the time-dependent raw data to the kinetic trace. In measuring kinetics, the fundamental quantity of interest is the kinetic trace, defined as the product flux as a function of the reaction time. Of course, kinetic traces for reactant loss and transient populations of intermediates can also be of interest, but for simplicity we consider here only the appearance of the product.

The oxidation of CO at platinum exemplifies the challenges in obtaining this quantity experimentally. As the reaction is initiated by CO adsorption, it is usual to use pulsed molecular beam methods. Time is required for CO oxidation to take place and for the product, CO_2, to desorb from the surface. The time at which the product appears at a detector is then recorded with respect to the reaction-initiating CO pulse. Hence, the time dependence of the raw signal obtained in this experiment is composed of three contributions: the time required for the CO pulse to travel to the surface, the reaction time at the surface, and the time required for the products to travel to the ionizing spot created by the laser. Only the second time period is of interest in a kinetics experiment. The first is identical for the two reaction channels and therefore only relevant to the determination of the time at which the reaction is initiated. Finally, the third time period is different for each of the two reaction channels and must be measured.

In velocity-resolved kinetics we measure ion images such as those shown in Extended Data Fig. 1a for each time delay between the CO and ionizing laser pulses. Here, the signal intensity is proportional to the CO_2 number density; as such, the hyperthermal channel (red box) is only weakly seen.

Multiplying the intensity by the velocity converts the density image to a CO_2 product flux image (Extended Data Fig. 1b). We then select velocity integration windows (green/blue and red rectangles in Extended Data Fig. 1) and record the average intensity versus the delay between the CO pulse and the ionizing laser pulse, producing raw kinetic traces. Extended Data Fig. 1c, d shows how this appears as a density signal and as flux, respectively.

Extended Data Fig. 2a shows the velocity distribution of the product CO_2, and can be decomposed into two contributions: thermal (blue) and hyperthermal (red). The velocity windows used for integration in Extended Data Fig. 1 are also shown (blue and red hatched areas). The kinetic traces are then scaled to represent the actual area under the fit to the velocity distribution (blue and red shaded areas).

A measurement of the angular distribution (Extended Data Fig. 2b, c) shows that the thermal CO_2 follows a cosine distribution, whereas the hyperthermal CO_2 follows a $\cos^8$ distribution, in agreement with previous reports[11–13,31].

The velocity distribution in Extended Data Fig. 2a includes only ions observed within 3° of the surface normal. In order for the kinetic traces to represent the total flux over all angles, we must scale up the kinetic trace of the thermal channel by an angular factor:

$$\frac{\int_0^{3^\circ} \cos^8\theta \sin\theta \mathrm{d}\theta}{\int_0^{90^\circ} \cos^8\theta \sin\theta \mathrm{d}\theta} \div \frac{\int_0^{3^\circ} \cos\theta \sin\theta \mathrm{d}\theta}{\int_0^{90^\circ} \cos\theta \sin\theta \mathrm{d}\theta} = 4.7$$

Note that in Extended Data Fig. 1d, the signal of the hyperthermal channel appears earlier than that of the thermal channel. This is a consequence of the reduced flight time of hyperthermal CO_2 to the ionizing laser spot, relative to that of the thermal CO_2. By subtracting the flight time using the average velocity associated with the integration window of each channel (12 and 35 μs, respectively), we can correct this. See Extended Data Fig. 2d, in which we have also shifted the zero of time to the onset of the CO adsorption. The temporal shape of the CO dosing pulse is measured as described in ref. [27].

Effective lifetimes as a function of oxygen coverage and step-dependent desorption. We perform a preliminary and approximate data analysis at low oxygen coverages, deriving effective lifetimes for each reaction channel, which leads to insights into the reaction mechanism. Extended Data Fig. 3a shows an example of the analysis. Here, the effective lifetime of the two reaction channels is derived through a simple exponential fit to the kinetic traces, convoluted over the time profile of the pulsed molecular beam.

The lifetimes obtained from the fits are effective values, $\tau_{\mathrm{eff}} = 1/k_{\mathrm{eff}}$, which depend on the total oxygen coverage $[O_a]$. The CO doses here are so small (less than 0.1% of a monolayer) that $[O_a]$ is independent of time during all transients. Referring to Extended Data Fig. 3b, it can be shown that $k_{\mathrm{eff}} = k_0 + k_2[O_a]$, where k_2 is the rate constant of the oxidation reaction and k_0 is a non-reactive competitive process removing the reactant CO, for example CO desorption.

With this mechanism, a simple set of differential equations can be solved analytically. This enables us to define the effective lifetime:

$$-\frac{\mathrm{d}[CO_a]}{\mathrm{d}t} = k_0[CO_a] + k_2[CO_a][O_a] = [CO_a](k_0 + k_2[O_a]) = [CO_a]k_{\mathrm{eff}}$$

$$[CO_a]_t = [CO_a]_0 \mathrm{e}^{-k_{\mathrm{eff}}t}$$

$$\mathrm{Flux}(CO_2) = k_2[O_a][CO_a]_t = k_2[O_a][CO_a]_0 \mathrm{e}^{-k_{\mathrm{eff}}t}$$

By varying the repetition rates of the two pulsed beams, we vary the fluxes of CO and O_2 and thereby the coverage of oxygen. Note that the use of repetition rate gives us very precise control of the fluxes. Methods section 'Total oxygen coverage, $[O_a]$, from a titration experiment' shows how the oxygen coverage is derived. In this way, we can observe a linear dependence between k_{eff} and the O_2 flux at low O_2 fluxes. Extended Data Fig. 3c shows an example of how $k_{\mathrm{eff}}^{\mathrm{thermal}}$ depends on the oxygen flux at several surface temperatures.

For each temperature, we extract k_0^{thermal} from the zero-coverage intercept of the linear fit. These are shown as filled circles in Extended Data Fig. 4, where they are compared to literature rate constants for CO desorption from Pt(111) steps (plus signs and filled circles) and terraces (triangles). The values of k_0^{thermal} derived here are in excellent agreement with desorption rate constants for CO adsorbed at steps.

Similar analysis for the hyperthermal channel on Pt(332) also reveals a non-reactive competitive channel that removes CO, $k_1^{\mathrm{hyperthermal}}$, which is consistent with CO diffusion across terraces together with desorption.

DFT calculation of minimum energy path for the terrace reaction. We performed DFT calculations within the generalized gradient approximation using the aimsChain tool within the FHI-aims package[32] to map out the minimum energy path of the CO oxidation reaction on Pt(111) terraces. The calculation used the RPBE functional in the spin-unpolarized (restricted) formalism with van der Waals corrections[33]. Other details of the calculations are as follows: A p(3 × 3) cell with 4 layers with an optimized lattice constant of 4.00 Å was used as a model for the Pt(111) surface. To find the initial and final state for the minimum energy path (MEP) calculation, we carried out geometry optimizations in which just CO and oxygen atoms were allowed to move and all surface atoms were restricted to their equilibrium positions. The optimizations were stopped when the force on every atom was <0.01 eV Å^{-1}. The minimum energy configurations found in this way were also checked against tight basis sets. For both MEP and geometry optimizations, the reciprocal space was sampled with a $4 \times 4 \times 1$ k-point grid, and to account for the electron occupation a Gaussian function with a width of 0.2 eV was used. The MEP calculations were performed using the string method[34] with light basis sets. To sample the MEP we have taken 15 images. The convergence of the pathway was reached when the forces between every image were smaller than 0.15 eV Å^{-1}. To determine the transition state more accurately, we used a force criterion of 0.05 eV Å^{-1} for the climbing image.

Extended Data Fig. 5 shows that the reaction is highly exoergic and passes over a substantial reaction barrier. The structure of the transition state is shown in the inset and is still far from the structure of the product, similar to that found in previous calculations[19,20]. This so-called 'early barrier' indicates that a substantial fraction of the reaction energy will be channelled into vibrational excitation of the product, CO_2.

We performed ab initio molecular dynamics calculations using the system and functional defined above, starting at the transition state determined from the MEP calculations to determine the translational energy of the product CO_2. The results from about 10 trajectories show that the values of the final translational energy are between 660 meV and 715 meV for the flexible slab at $T = 0$ K, and between 720 meV and 920 meV for the rigid slab. The results of this electronically adiabatic calculation are consistent with those of experiments, in which molecular energy may also be shared with the electron–hole pairs of the metal.

Kinetic modelling of the velocity-resolved data for CO oxidation on Pt(111). *Reaction scheme.* The kinetic model is based on the following reaction scheme for CO oxidation:

$$CO_{Beam} + S_{Step} \xrightarrow{s_{CO}} CO_{Step} \quad \text{Step adsorption} \quad (1)$$

$$CO_{Beam} + S_{Terr} \xrightarrow{s_{CO}} CO_{Terr} \quad \text{Terrace adsorption} \quad (2)$$

$$CO_{Terr} + S_{Step} \xrightarrow{k_1^{TS}} CO_{Step} + S_{Terr} \quad \text{Diffusion} \quad (3)$$

$$CO_{Terr} \xrightarrow{k_0^{T}} CO_g + S_{Terr} \quad \text{Terrace desorption} \quad (4)$$

$$CO_{Step} \xrightarrow{k_0^{S}} CO_g + S_{Step} \quad \text{Step desorption} \quad (5)$$

$$CO_{Terr} + O_{Terr} \xrightarrow{k_2^{TT}} CO_{2,g}^{hyperthermal} + 2S_{Terr} \quad \text{TT reaction} \quad (6)$$

$$CO_{Terr} + O_{Step} \xrightarrow{k_2^{TS}} CO_{2,g}^{thermal} + S_{Terr} + S_{Step} \quad \text{TS reaction} \quad (7)$$

$$CO_{Step} + O_{Step} \xrightarrow{k_2^{SS}} CO_{2,g}^{thermal} + 2S_{Step} \quad \text{SS reaction} \quad (8)$$

where $S_{Terr,Step}$ are the free sites expressed in monolayers. Because the step density is less than 1% on our Pt(111) sample, we omit reaction (1) and consider only CO adsorption at terraces. We include reaction (1) for completeness and it will be important for our treatment of Pt(332). The diffusion from steps back to terraces has been omitted; as we see different temporal behaviour of the two kinetic traces in Extended Data Fig. 1, we conclude that the two CO species are not in fast equilibrium with each other. The diffusion from steps back onto the terrace must therefore be slow compared to the other processes.

The rate equations describing this mechanism are as follows:

$$\frac{d[O_{Step}]}{dt} = -(k_2^{TS}[CO_{Terr}] + k_2^{SS}[CO_{Step}])\frac{[O_{Step}]}{d_{Step}}$$

$$\frac{d[CO_{Step}]}{dt} = -\left(k_0^{S} + k_2^{SS}\frac{[O_{Step}]}{d_{Step}}\right)[CO_{Step}] + k_1^{TS}[CO_{Terr}]\frac{d_{Step} - [O_{Step}] - [CO_{Step}]}{d_{Step}}$$

$$\frac{d[CO_{Terr}]}{dt} = -\left(k_0^{T} + k_1^{TS}\frac{d_{Step} - [O_{Step}] - [CO_{Step}]}{d_{Step}} + k_2^{TT}\frac{[O_{Terr}]}{d_{Terr}} + k_2^{TS}\frac{[O_{Step}]}{d_{Step}}\right)[CO_{Terr}]$$

$$|Flux(CO_{2,g}^{thermal})| = k_2^{TS}[CO_{Terr}]\frac{[O_{Step}]}{d_{Step}} + k_2^{SS}[CO_{Step}]\frac{[O_{Step}]}{d_{Step}}$$

$$|Flux(CO_{2,g}^{hyperthermal})| = k_2^{TT}[CO_{Terr}]\frac{[O_{Terr}]}{d_{Terr}}$$

where the square brackets refer to concentration in monolayers of surface-adsorbed reactants and products with respect to the entire surface, d_{Step} and d_{Terr} are the concentrations of the step and terrace sites expressed in monolayers with respect to the entire surface that is, $d_{Step} + d_{Terr} = 1$ monolayer, $|Flux(CO_{2,g})|$ refers to the absolute value of the flux of $CO_{2,g}$ gas phase product molecules. All rate constants k are in units of s^{-1}.

We stress here that when probing the gas-phase product from a surface reaction, the flux of this species must be measured and not the rate of change of the product density, $d[CO_{2,g}]/dt$. A simple dimensional analysis of the rate law clarifies this point:

$$k_2^{TT}[CO_{Terr}]\frac{[O_{Terr}]}{d_{Terr}} \quad \text{has units of} \quad \frac{\text{monolayers}}{s} \propto \frac{\text{particles}}{cm^2\,s}$$

while

$$\frac{d[CO_{2,g}]}{dt} \quad \text{has units of} \quad \frac{\text{particles}}{cm^3\,s}$$

Flux has, by definition, units of particles $cm^{-2}\,s^{-1}$.

The physical picture that further confirms this is the fact that as the particles desorb from a two-dimensional surface area, after some time they occupy a certain volume. This volume is proportional to the velocity. Measuring simply the density of the particles is insufficient, as high-speed and low-speed particles will have 'expanded' into different volumes.

Ion imaging can therefore function as a flux detector and, as such, is ideally suited for the measurement of kinetics at surfaces that result in gas-phase products.

Numerical solution to the kinetic model. We derive a system of ordinary differential equations for the reaction scheme above and solve them numerically. The initial values for the concentration of oxygen, that is, $[O_{Terr}]$ and $[O_{Step}]$, are provided as an initial guess from the titration data (see Methods section 'Validation of $[O_{Terr}]$ and $[O_{Step}]$ from the numerical solution'). The concentration of free sites, $[S_{Terr}]$ and $[S_{Step}]$, are expressed in units of monolayers, that is, $[S_{Terr}] = 0.9975$ monolayers and $[S_{Terr}] = 0.0025$ monolayers for an empty surface and a step density of 0.25% as determined from AFM measurements. The rate constants for desorption from steps and terraces are known from previous experiments, and the rate constant for diffusion is estimated from literature values. An initial guess for the rate constants of the reaction is provided from an analysis of k_{eff} (see Methods section 'Effective lifetimes as a function of oxygen coverage and step-dependent desorption'). The adsorption of CO from the incoming beam is then introduced as a perturbation to this system.

Optimization process. The flux of CO_2 into the thermal and hyperthermal channels as a function of time was then obtained by solving the ordinary-differential-equation system using LSODA from the FORTRAN77 library ODEPACK[35]. This flux was compared to the experimental data and the residuals were minimized in a recursive optimization. We used four global parameters, k_1^{TS}, k_2^{TT}, k_2^{TS} and k_2^{SS}, and two local parameters per dataset, the concentration of $[O_{Terr}]$ and $[O_{Step}]$, to perform optimization with the Nelder–Mead method. Following ref. [36], $[O_{Step}]$ can occupy every second (fcc) platinum-step site, therefore the maximum of $[O_{Step}]$ was restricted to $<0.5d_S$.

Using these four global parameters, the kinetic model was able to properly reproduce 18 sets of thermal and hyperthermal flux at 7 temperatures, a total of 252 kinetic traces. Examples are shown in Extended Data Fig. 6.

Total oxygen coverage, $[O_a]$, from a titration experiment. The total amount of oxygen on the surface, $[O_a]$, could be determined in a titration experiment. First, a surface fully covered with oxygen (0.25 monolayers) was continuously dosed with CO and the total CO_2 yield was measured. Next, the CO and O_2 beams were run at a value of RRR used when measuring kinetic traces; this established a steady-state oxygen coverage. After several minutes, the O_2 beam was suddenly turned off and the total CO_2 yield was again measured. This CO_2 yield was then compared to the yield obtained from a fully covered surface, allowing us to relate RRR to the resulting steady-state oxygen coverage. The result is shown as black squares in Extended Data Fig. 7a.

Validation of $[O_{Terr}]$ and $[O_{Step}]$ from the numerical solution. To test whether the values for $[O_{Terr}]$ and $[O_{Step}]$ obtained from the numerical model are reasonable, we compare their sum to the total amount of oxygen on the surface as obtained from the titration experiments just described. The kinetic model result for $[O_a]$ is plotted as red dots in Extended Data Fig. 7a. The good agreement between the prediction of the numerical solution and the titration determined values of oxygen coverage validates the way in which the numerical model deals with the oxygen coverage.

In addition to this, we want to confirm that the partitioning of $[O_a]$ into $[O_{Terr}]$ and $[O_{Step}]$ is reasonable. The equilibrium between the two oxygen species is calculated using the canonical partition function for oxygen atoms distributed among step and terrace sites using a given energy difference as described in Methods section 'Equilibrium calculation of oxygen-atom populations at steps and terraces'. The step coverage is defined as

$$\theta_{Step} = \frac{[O_{Step}]}{0.5d_{Step}}$$

with the step density $d_{Step} = 0.0025$. As explained in Methods section 'Optimization process', one oxygen atom occupies every second binding site, therefore the factor of 0.5 is used.

A plot comparing the numerical results to the equilibrium expectation is shown in Extended Data Fig. 7b. Here the relative binding energy of oxygen at steps and terraces was varied between 0.05 and 0.16 eV. Theoretical calculations using DFT suggest that step oxygen is more strongly bound than terrace oxygen, by about 0.26 eV[30,37].

Therefore, the data suggests that the equilibrium distribution of oxygen atoms between steps and terraces is not established. Given the slow diffusion speeds on Pt(111) at our temperatures and the large average terrace size of about 400 atoms, this is conceivable. The distribution on Pt(332), which has an average terrace length of only five atoms, appears closer to or at equilibrium (see Methods section 'Kinetic studies of CO oxidation on Pt(332)').

Equilibrium calculation of oxygen-atom populations at steps and terraces. In developing the numerical model for the oxidation of CO on platinum, we must account for the partitioning of oxygen atoms between steps and terraces. Theoretical calculations using DFT suggest that step-bound oxygen is more strongly bound than terrace-bound oxygen (by about 0.26 eV[30,37]). One limiting approach to this problem is equilibrium partitioning.

Whereas step-bound oxygen is favoured by energetic considerations, terrace-bound oxygen atoms are favoured by entropy. To describe this, we have used a simple expression for the equilibrium constant which can be derived from the canonical partition function of non-interacting oxygen atoms bound at two sites (steps and terraces):

$$Q(n_{\mathrm{Step}}, n_{\mathrm{Terr}}, n_{\mathrm{O}}, E_{ts}, \beta) = \sum_{m=0}^{n_{\mathrm{Step}}} \binom{n_{\mathrm{Step}}}{m} \binom{n_{\mathrm{Terr}}}{n_{\mathrm{O}}-m} \mathrm{e}^{-\beta((n_{\mathrm{O}}-m)E_{ts}-E_0)}$$

Here, binomial coefficients are used to calculate the number of ways to distribute n_O oxygen atoms over n step sites (n_{step}) and n terrace sites (n_{terr}). We take into account that saturated coverage of steps occurs at a 2:1 ratio of platinum to oxygen atoms, whereas saturation of terraces occurs at a 4:1 ratio. E_{TS} is the energetic stability difference between step-bound oxygen atoms and terrace-bound oxygen atoms. If we use this equilibrium partitioning to characterize our experimentally derived results by allowing E_{TS} to vary, we find a value that depends on step density. For Pt(111) we find $E_{TS} = 0.05$ eV (see Methods section 'Validation of [O_{Terr}] and [O_{Step}] from the numerical solution'), whereas for Pt(332) we find $E_{TS} = 0.12$ eV (see Methods section 'Kinetic studies of CO oxidation on Pt(332)'). We observe that the E_{TS} for Pt(332) is closer to that obtained from the DFT calculations[30,37], which could suggest that the system on the (332) surface is closer to equilibrium.

Kinetic studies of CO oxidation on Pt(332). The kinetic mechanism for CO oxidation on Pt(332) is identical to that described in Methods section 'Reaction scheme' for Pt(111); however, here the step density (0.167) is large. Therefore, we include both reactions (1) and (2) weighted by 0.167 and 0.833, respectively. Based on our success with the treatment of the Pt(111) data, we implemented the numerical model as follows.

First, we used titration measurements as described in Methods section 'Total oxygen coverage, [O_a], from a titration experiment' as a starting point for the determination of the total oxygen coverage as a function of the ratio of O_2 to CO fluxes (Extended Data Fig. 7c). We then constructed limits (red shaded area in Extended Data Fig. 7c) within which the oxygen coverage could be varied in the numerical optimization to reflect the uncertainty of the titration measurements. For the initial conditions of the numerical optimization, we assume the partitioning of oxygen between steps and terraces is at equilibrium as discussed in Methods section 'Validation of [O_{Terr}] and [O_{Step}] from the numerical solution'. After the fitting of the data is complete, the partitioning of the oxygen atoms at steps and terraces has also been optimized and is shown as black triangles in Extended Data Fig. 7d. These are compared to equilibrium calculations assuming different values of the binding energy difference between oxygen atoms at steps and terraces. The results obtained from the numerical fit are similar to equilibrium values when the energetic preference for step-bound oxygen atoms was 0.10–0.14 eV. Compared to the results derived from the Pt(111) experiments, this value is much closer to the theoretically estimated difference in binding energy. This is probably due to much smaller terrace sizes leading to faster equilibration compared to Pt(111).

Extended Data Fig. 8 shows examples of the quality of the fit obtained using the rate constants from Table 1. We emphasize that both reactions (7) and (8)—the terrace–step and step–step reactions, respectively—are necessary to account for the biexponential fall-off in the thermal channel. Furthermore, the magnitudes of the rate constants obtained from the Pt(111) and Pt(332) surfaces are in excellent agreement; see Fig. 3 and Table 1.

We point out that the derived activation energies for the three reactions make intuitive sense. For early-barrier reactions, the relative energies of the transition states follow closely the relative energies of the reactants. For the TT reaction, our experimental activation energy is 0.6 ± 0.1 eV. In considering the SS reaction, the step-bound oxygen atom is stabilized by about 0.15 eV (see Methods section 'Equilibrium calculation of oxygen-atom populations at steps and terraces') and the step-bound CO is stabilized by 0.16–0.35 eV[38–40]. Here there are a variety of experimental studies that give a range of results. For early-barrier reactions, the transition state is stabilized by a similar amount of energy as the reactants are stabilized. Therefore it is not surprising that the SS reaction has a similar activation energy (0.65 ± 0.1eV) to that of the TT reaction (0.6 ± 0.1 eV). We speculate that the TS reaction and the SS reaction access the same transition state via two different reactant geometries. If true, the activation energy for the TS reaction would be lowered by the step-to-terrace relative binding energy of CO, which is 0.16–0.3 eV. This simple analysis would predict a lower activation energy for the TS reaction of anywhere between 0.49 and 0.25 eV, which is consistent with our experimentally derived value of 0.4 ± 0.1 eV.

Comparison of velocity-resolved kinetics to previous reported velocity-integrated kinetic results. Previous surface-kinetics experiments were not able to resolve product velocities. Furthermore, only a single oxidation reaction was assumed, enabling a pseudo-first order analysis as a function of the surface temperature T_S and [O_a], from which activation energies were derived. Extended Data Fig. 9b shows reported activation energies versus [O_a] for the reaction thought to result from CO oxidation at terraces (hollow circles and plus signs) from refs [7,41].

We can use our velocity-resolved data to simulate these previous results. We integrate the kinetic trace over the product velocities and fit it as if pseudo-first-order kinetics applied (see Extended Data Fig. 9a). We do this for data at many temperatures and values of [O_a]. The apparent activation energies obtained in this way are shown as filled circles in Extended Data Fig. 9b, and there is marked agreement with the results of previous work.

We emphasize that the true oxidation kinetics involves three reactions, the activation energies of which are independent of [O_a]. This exemplifies how velocity-resolved kinetics removes a layer of averaging that confounds accurate kinetic analysis.

The interpretations of previous work suggested that the activation energy of a surface reaction could vary continuously with coverage, leading to a change of more than 0.5 eV owing to oxygen-atom occupation of neighbouring reaction sites at a distance of around 8 Å or more. This is clearly not the case. It is notable that the assumption of the single-reaction mechanism leads to this erroneous conclusion.

Temperature dependence of the site-specific mechanism. We used the numerical model with rate parameters that have been optimized to reproduce the velocity-resolved kinetics data to explore the behaviour of CO oxidation as a function of temperature and oxygen coverage. Extended Data Fig. 10a shows the CO oxidation efficiency (probability that an adsorbed CO molecule is converted to CO_2). Extended Data Fig. 10b shows the relative fraction of the hyperthermal channel (TT reaction) with respect to the thermal channels (TS and SS).

We note that the dominant role of step reactions between 500 and 700 K may appear inconsistent with Fig. 3, which shows $k_2^{TT} > k_2^{SS}, k_2^{TS}$ in this temperature range. This points out how subtle the kinetics of CO oxidation can be. Although the TT reaction has a higher rate constant, it must compete with CO diffusion to steps, which is faster than the terrace reaction at these temperatures. Furthermore, CO is preferentially adsorbed at steps; as such, it does not so easily diffuse back to the terraces once it has arrived at a step. Although it is true that step reactions have lower rate constants than do terrace reactions, CO molecules that have arrived at steps may only either react or desorb. Because desorption is rather slow, the reaction dominates. Another factor that is especially important when the total oxygen coverage is low is that oxygen atoms are preferentially found at step sites, which obviously favours reaction at steps.

Therefore, the relative importance of step and terrace reactions is strongly influenced by diffusion and desorption. Under conditions in which the TT reaction dominates, the reaction probability of conversion from CO to CO_2 is small. We explain this by observing that the TT reaction can only dominate when CO desorption is faster than CO diffusion. Under such conditions, desorption is also faster than the TT reaction. We note that this is consistent with previous observations, in which only the hyperthermal channel was seen[8]. We have carried out similar calculations for the Pt(332) catalysts with step densities of 16.7%, and the results are nearly identical.

It is also interesting to note that many industrial catalysts are used in a temperature region in which the CO–CO_2 conversion efficiency is low.

Sensitivity analysis. The three lower panels in Extended Data Fig. 10 show how the fit to the data (represented by the total fit residual $|\chi|$) depends on the three activation energies derived from our numerical model. Each two-dimensional contour plot shows sensitivity and the potential correlation of fitting error between two fitting parameters.

The total fit residual was obtained by summing over the array containing the residual at each data point for both channels under 152 different reaction

conditions (both temperature and oxygen coverage vary within the dataset). The Nelder–Mead optimization method used the same residual array as input. For each point within each contour plot, the activation energies were varied as indicated by the respective axis. The reported energy was varied by ±0.2 eV in steps of 0.013 eV. The pre-exponential factors were adjusted to compensate for the effect of the change in activation energy in the middle of the temperature range of the experiments (320 °C). In other words, when varying the activation energy, the rate constant at 320 °C was kept constant by compensating the prefactor.

We can make a number of observations from these three plots. First, the residual is more sensitive to changes of E_a^{TS} than it is to the other two activation energies. This can be seen from the strong gradient along the horizontal direction in Extended Data Fig. 10c and the large curvature along the vertical axis in Extended Data Fig. 10d. Second, E_a^{TT} (the vertical axis of Extended Data Fig. 10c) and E_a^{SS} (the horizontal axis of Extended Data Fig. 10d) are ineffective at compensating fit error when E_a^{TS} is shifted away from its optimal value. Hence both plots appear as long and narrow valleys aligned with one of the two axes. This reflects the small correlation between these fitting parameters; the slant in Extended Data Fig. 10d represents a weak correlation in fitting error between E_a^{TS} and E_a^{SS}. Extended Data Fig. 10e shows the sensitivity of E_a^{TT} and E_a^{SS} and correlation error involved in the fitting. From this plot we can see that the reported activation energies indeed reflect the minimum residual and that the residuals depend approximately equally on E_a^{TT} and E_a^{SS}. The approximately circular form of this contour plot indicates that the two fitting degrees of freedom are approximately uncorrelated with one another and that an optimized fit is sensitive to both activation energies.

On the basis of this analysis, we suggest an uncertainty of 0.05–0.1 eV for E_a^{TS} and an uncertainty of 0.1–0.2 eV for E_a^{TT} and E_a^{SS}.

Data availability. The data that support the findings of this study are available from the corresponding author upon reasonable request.

31. Poehlmann, E., Schmitt, M., Hoinkes, H. & Wilsch, H. Velocity distributions of carbon dioxide molecules from the oxidation of CO on Pt(111). *Surf. Sci.* **287–288**, 269–272 (1993).
32. Blum, V. et al. Ab initio molecular simulations with numeric atom-centered orbitals. *Comput. Phys. Commun.* **180**, 2175–2196 (2009).
33. Tkatchenko, A. & Scheffler, M. Accurate molecular van der Waals interactions from ground-state electron density and free-atom reference data. *Phys. Rev. Lett.* **102**, 073005 (2009).
34. E, W., Ren, W. & Vanden-Eijnden, E. Simplified and improved string method for computing the minimum energy paths in barrier-crossing events. *J. Chem. Phys.* **126**, 164103 (2007).
35. Hindmarsh, A. C. in *Scientific Computing* (eds Stepleman, R. S. et al.) 55–64 (North-Holland, Amsterdam, 1983).
36. Gland, J. L. & Korchak, V. N. The adsorption of oxygen on a stepped platinum single crystal surface. *Surf. Sci.* **75**, 733–750 (1978).
37. Nagoya, A., Jinnouchi, R., Kodama, K. & Morimoto, Y. DFT calculations on H, OH and O adsorbate formations on Pt(322) electrode. *J. Electroanal. Chem.* **757**, 116–127 (2015).
38. Borodin, D. *Probing Reactions at Surfaces using Ion Imaging—CO Oxidation at Atomically Flat and Stepped Surfaces of Platinum and Palladium*. MSc thesis, Georg-August Univ. Göttingen (2017).
39. Reutt-Robey, J. E., Doren, D. J., Chabal, Y. J. & Christman, S. B. Microscopic CO diffusion on a Pt(111) surface by time-resolved infrared spectroscopy. *Phys. Rev. Lett.* **61**, 2778–2781 (1988).
40. Lin, T. H. & Somorjai, G. A. Modulated molecular beam scattering of CO and NO from Pt(111) and the stepped Pt(557) crystal surfaces. *Surf. Sci.* **107**, 573–585 (1981).
41. Gland, J. L. & Kollin, E. B. Carbon monoxide oxidation on the Pt(111) surface: Temperature programmed reaction of coadsorbed atomic oxygen and carbon monoxide. *J. Chem. Phys.* **78**, 963 (1983).
42. Janda, K. C. et al. Direct measurement of velocity distributions in argon beam–tungsten surface scattering. *J. Chem. Phys.* **72**, 2403 (1980).
43. Verheij, L. K., Lux, J., Anton, A. B., Poelsema, B. & Comsa, G. A molecular beam study of the interaction of CO molecules with a Pt(111) surface using pulse shape analysis. *Surf. Sci.* **182**, 390–410 (1987).

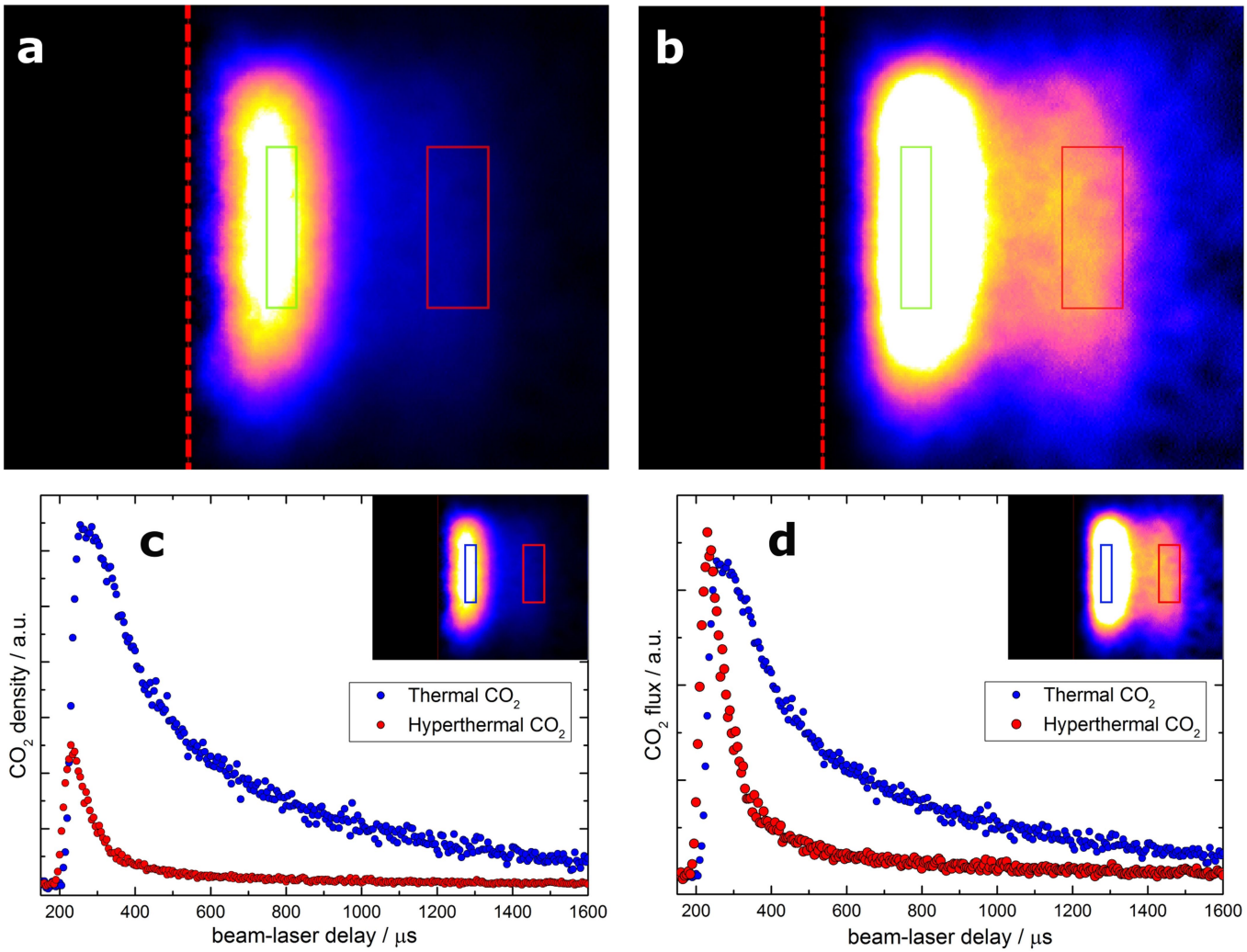

Extended Data Fig. 1 | Kinetics of CO_2 formation. a, **b**, Ion images of the product CO_2. **a**, Raw data after background subtraction, with the intensity of each pixel proportional to the density of CO_2. The pixel distance from the laser position (dashed red line) is proportional to the velocity, that is, velocity increases to the right. **b**, Data after multiplying each pixel by its corresponding velocity, with the resulting pixel intensity proportional to the flux and the hyperthermal channel then becoming more readily apparent. The red and green rectangles indicate typical velocity integration windows used to produce kinetic traces for the thermal and hyperthermal channels. The vertical span of the boxes subtends ±3° around the surface normal. This small angular range justifies using rectangular integration windows. For defining kinetic traces, we take the average intensity within the rectangles as the product flux normal to the surface. **c**, **d**, Raw kinetic trace data. **c**, Average density of the CO_2 product integrated over the blue (thermal channel) and red (hyperthermal channel) rectangular areas of the ion image (inset). **d**, Same data converted to flux. This kinetic trace and the ion images above were measured at 350 °C, a time-averaged CO flux of 2.2×10^{12} s^{-1} cm^{-2} and a time-averaged O_2 flux of 1.1×10^{13} s^{-1} cm^{-2}.

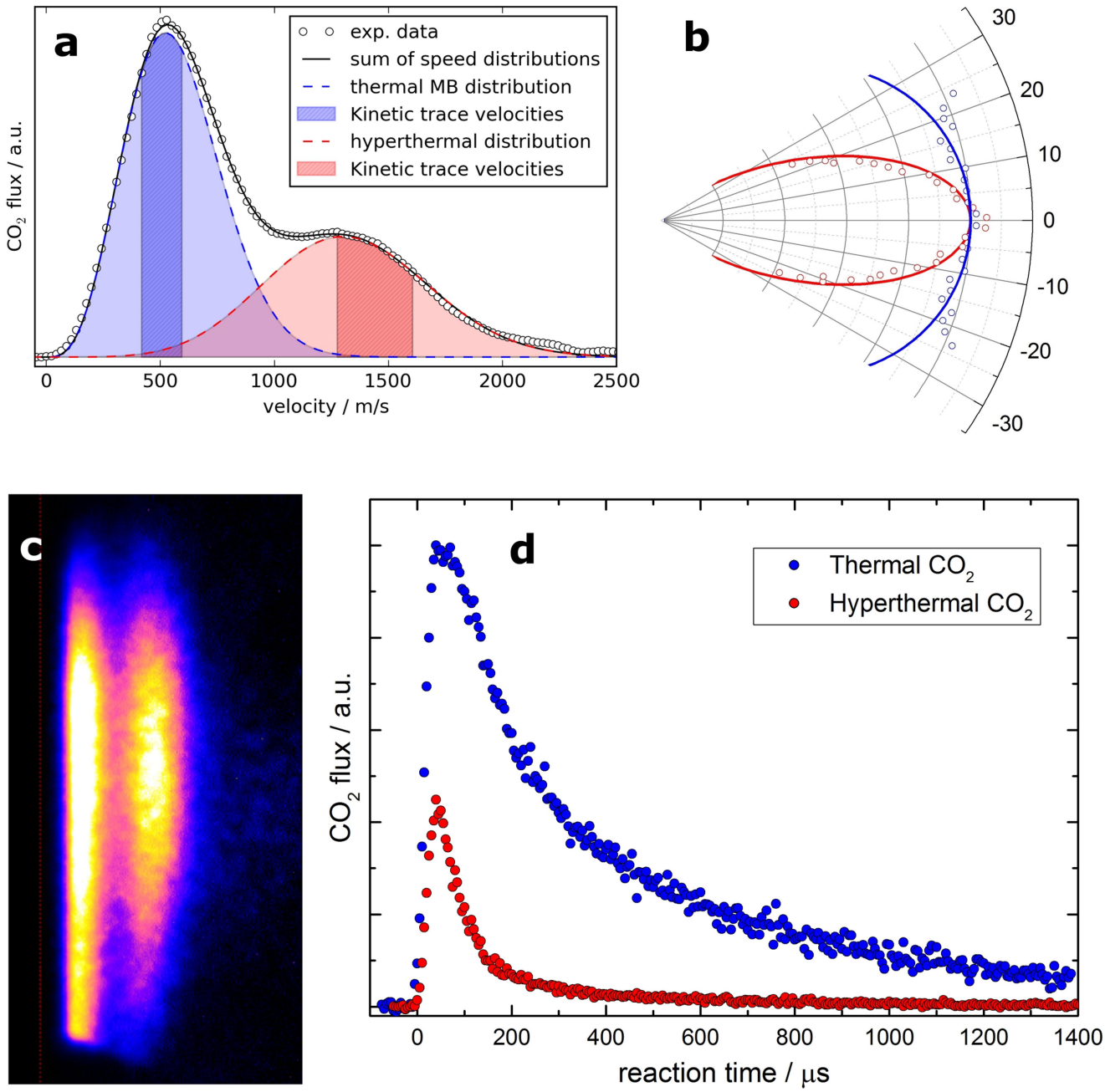

Extended Data Fig. 2 | Branching between thermal and hyperthermal reaction channels. a, Product speed distribution. The branching ratio between the thermal and hyperthermal channels is obtained from this distribution, calculated from the ion image in Extended Data Fig. 1. The thermal product channel is fit to a Maxwell–Boltzmann function (T_{trans} = 483 K; dashed blue line) and the hyperthermal channel is fit to a flowing Maxwell–Boltzmann function[42] (T_{trans} = 894 K, α = 190 meV; dashed red line). The velocities used for extraction of the kinetic traces are indicated by the hatched areas. **b**, The angular distribution for the ion image shown in **c**. **c**, The flux-corrected ion image that shows an angular distribution subtending ±25° around the surface normal. The angular distribution was measured at a surface temperature of 400 °C. **d**, The kinetic trace. We obtain the product flux as a function of reaction time for two channels with different speed and angular distributions (details are given in the text). It is now clear that the hyperthermal channel is much weaker than the thermal channel.

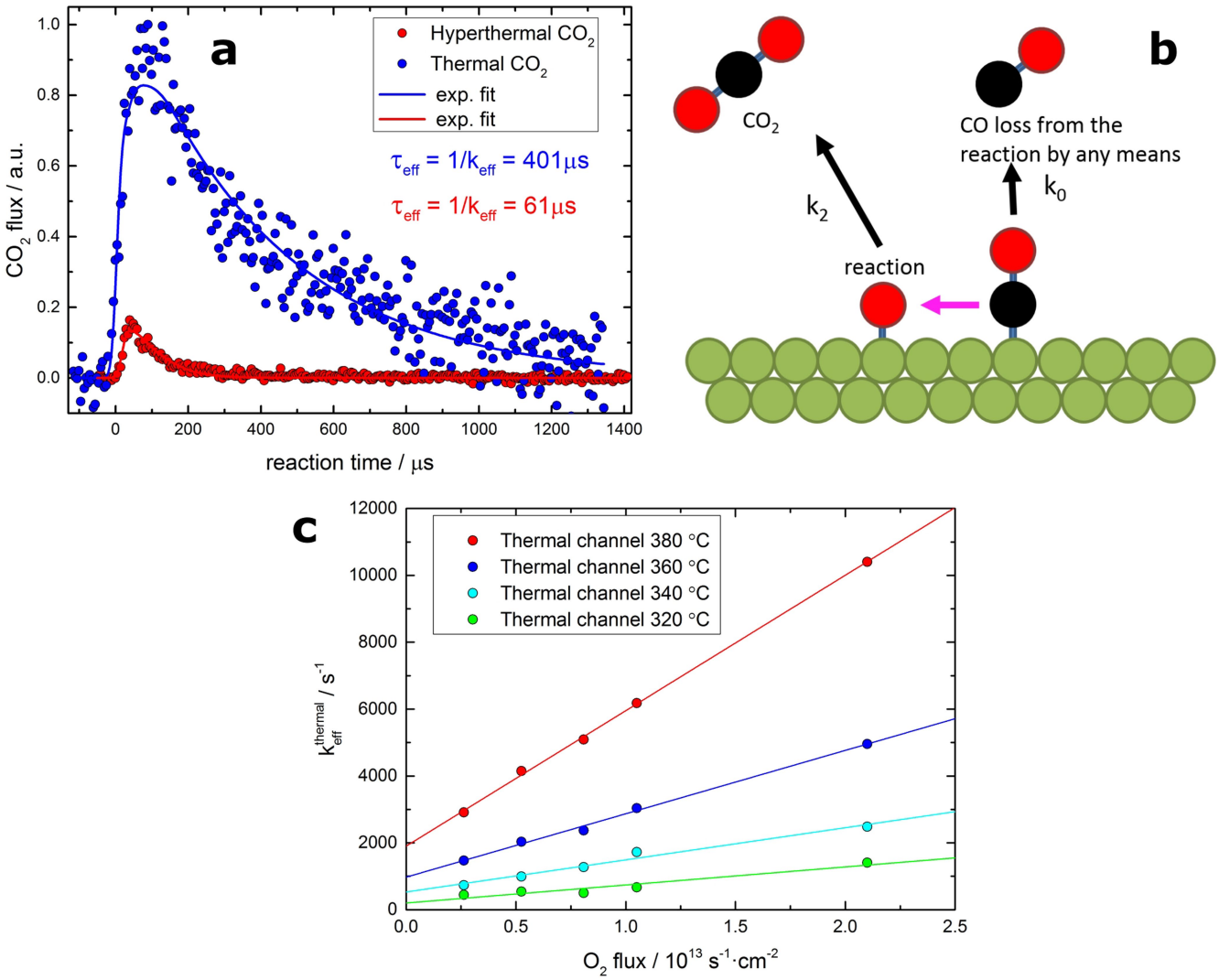

Extended Data Fig. 3 | Effective lifetime analysis. a, Kinetic traces of the thermal and the hyperthermal channel fitted by a convolution of an exponential decay over the incoming beam. **b**, Kinetic model for the effective lifetime of the thermal channel of CO oxidation. **c**, Effective lifetimes plotted against time-averaged O_2 flux. Solid circles are experimental points for $k_{eff}^{thermal}$. The *y*-intercept is non-zero owing to CO desorption. In these measurements, the time-averaged CO flux was 2.2×10^{12} s^{-1} cm^{-2}.

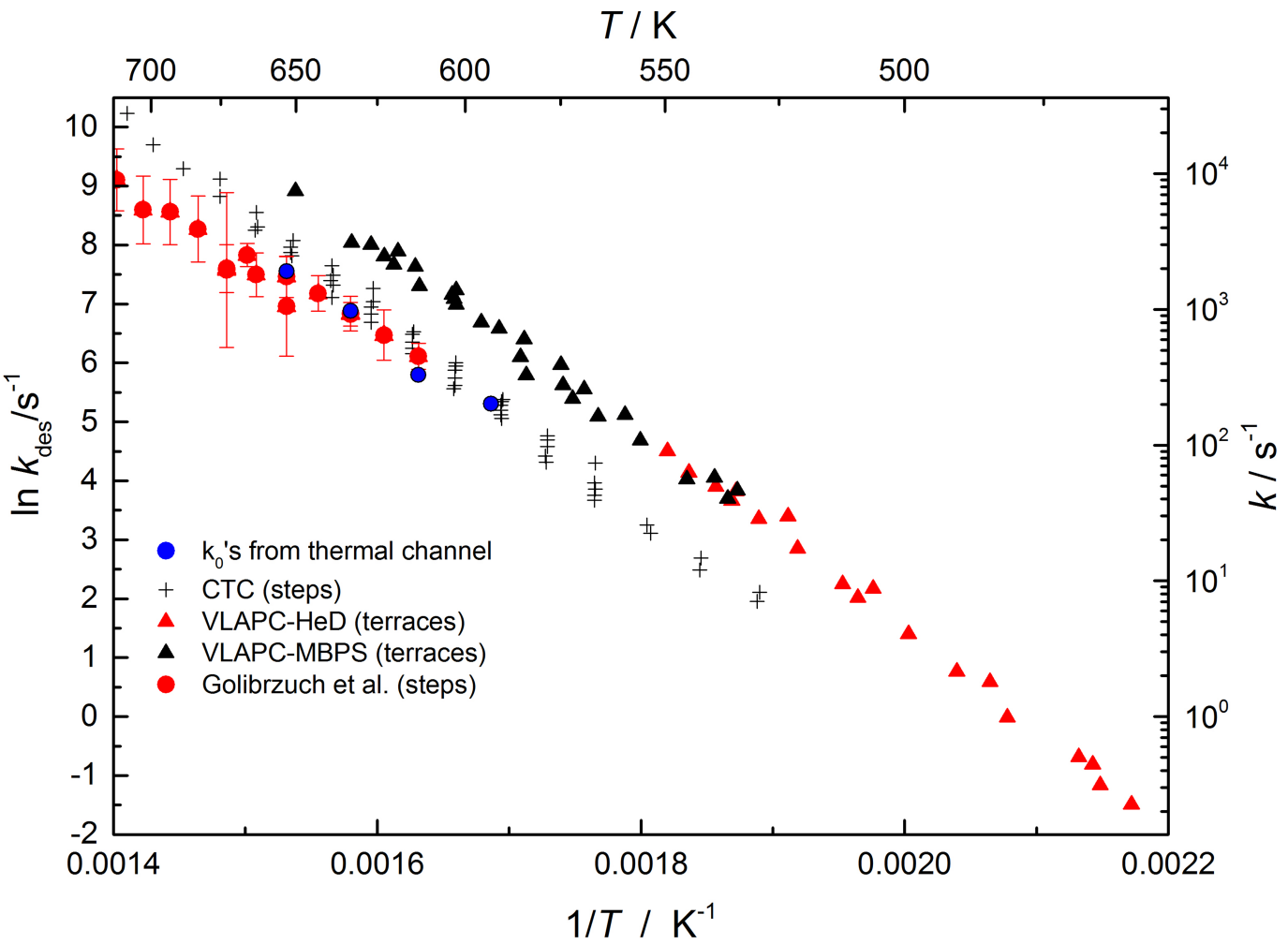

Extended Data Fig. 4 | Rate constants for CO desorption from Pt(111). Rate constants for desorption of CO from Pt(111) terraces (black and red triangles) are taken from ref. [43]. The plus signs are rate constants for desorption of CO from steps; see ref. [18]. The filled red circles show rate constants for desorption of CO from steps as measured previously[27]. The zero-coverage rate constants from Extended Data Fig. 3 are shown as filled blue circles.

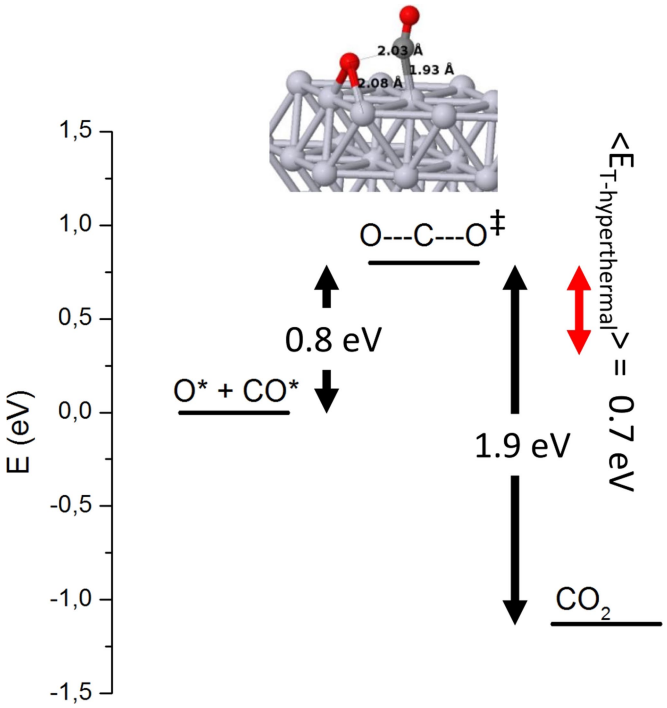

Extended Data Fig. 5 | Points along the reaction coordinate of the terrace–terrace reaction. The transition state resembles reactants; it is a so-called 'early-barrier' reaction. Such reactions channel the energy released in the reaction primarily into product vibration. Experimentally we observe that approximately 20% of the barrier-height energy (0.38 eV) appears as product transitional energy in the hyperthermal channel. We take this as evidence that the hyperthermal reaction takes place on platinum terraces.

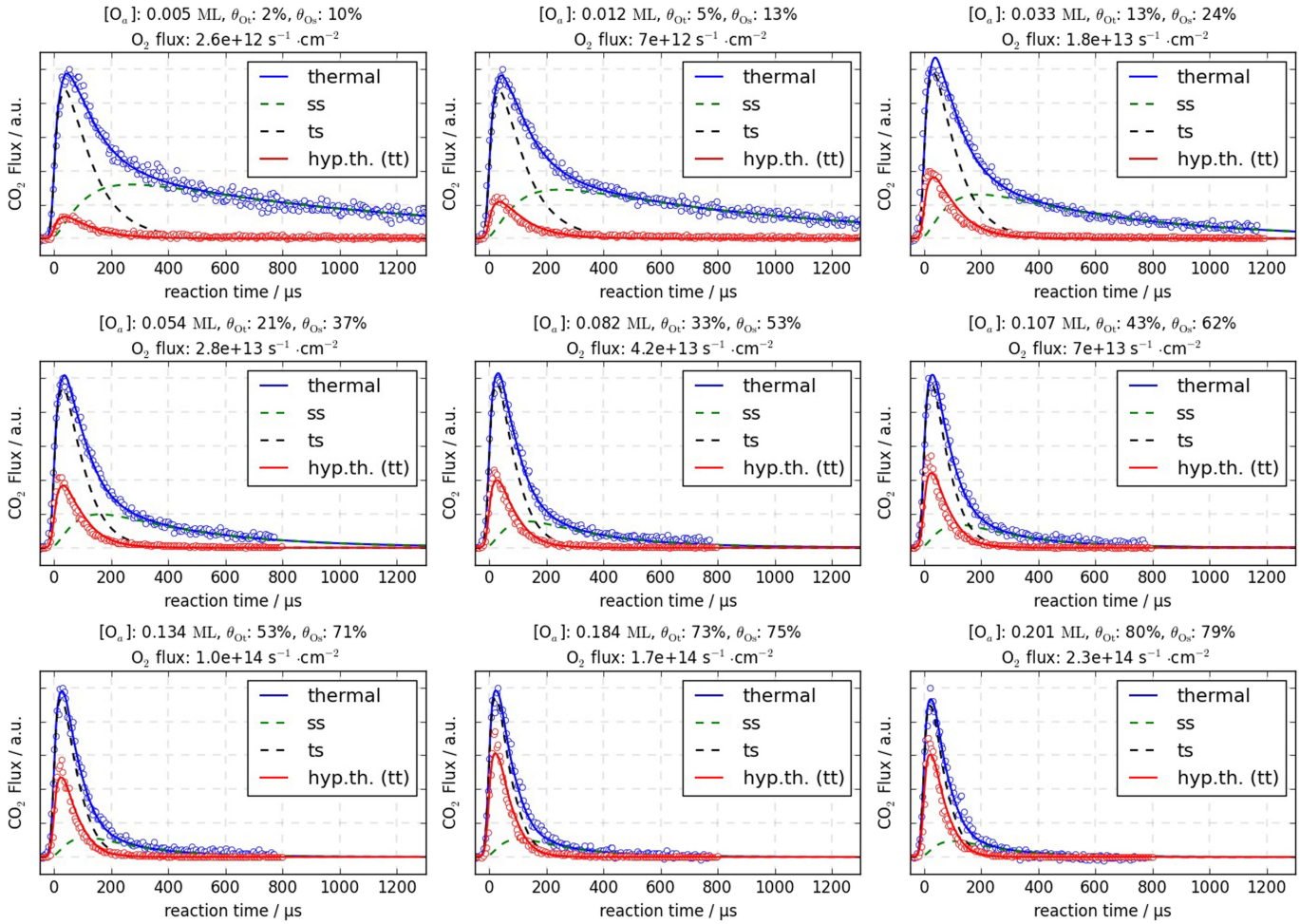

Extended Data Fig. 6 | Examples of the kinetic model fit to experimentally derived kinetic traces for Pt(111). Nine out of 18 (every second) kinetic traces at 340 °C are shown. Similar fit quality was obtained for 18 plots for seven temperatures between 290 and 350 °C. Information on the total oxygen coverage [O_a], the fractional coverage on steps and terraces (θ_{OT} and θ_{OS}, respectively) and the time-averaged O_2 flux is shown above each plot. The time-averaged CO flux was 2.2×10^{12} s^{-1} cm^{-2}.

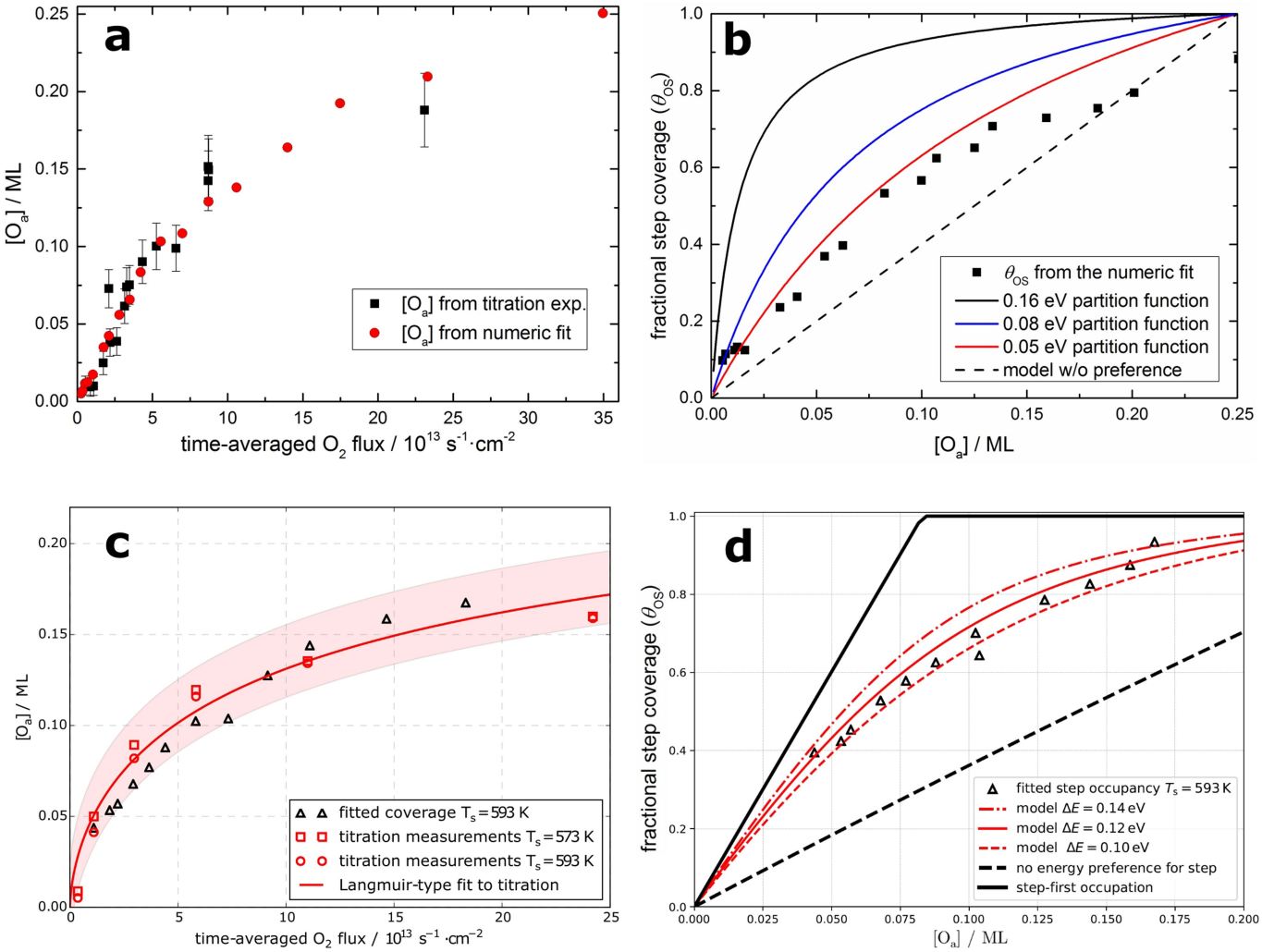

Extended Data Fig. 7 | Oxygen coverage on platinum surfaces. **a**, A comparison of the values of total adsorbed oxygen [O_a] obtained from titrations on Pt(111) with [O_a] values obtained from the numerical solution. The black squares with estimated uncertainty (1 s.d.) are the total amount of oxygen on the surface, [O_a], obtained from titration measurements. The red dots show [O_a] = [O_{Terr}] + [O_{Step}] obtained from the numerical solution at 340 °C. The time-averaged CO flux was 2.2×10^{12} s^{-1} cm^{-2}. **b**, The fractional step coverage (θ_{OS}) on Pt(111) from the numerical solution compared to the partition function simulation. The black squares are the result of the numerical fit shown in Extended Data Fig. 6. All data are at 340 °C. **c**, A comparison of values of [O_a] obtained from titrations on Pt(332) with [O_a] values obtained from the numerical kinetic model. Note that the titration results are found to be independent of surface temperature under our conditions. **d**, The fractional step coverage (θ_{OS}) plotted against [O_a] for Pt(332). The red lines are results from the partition function calculated for different binding energy differences. The black triangles are the results from the numerical analysis of the kinetic model. Two extreme cases—no oxygen-atom binding preference for steps (dashed) and large oxygen-atom binding preference for steps (solid)—for the partition function are shown as black lines.

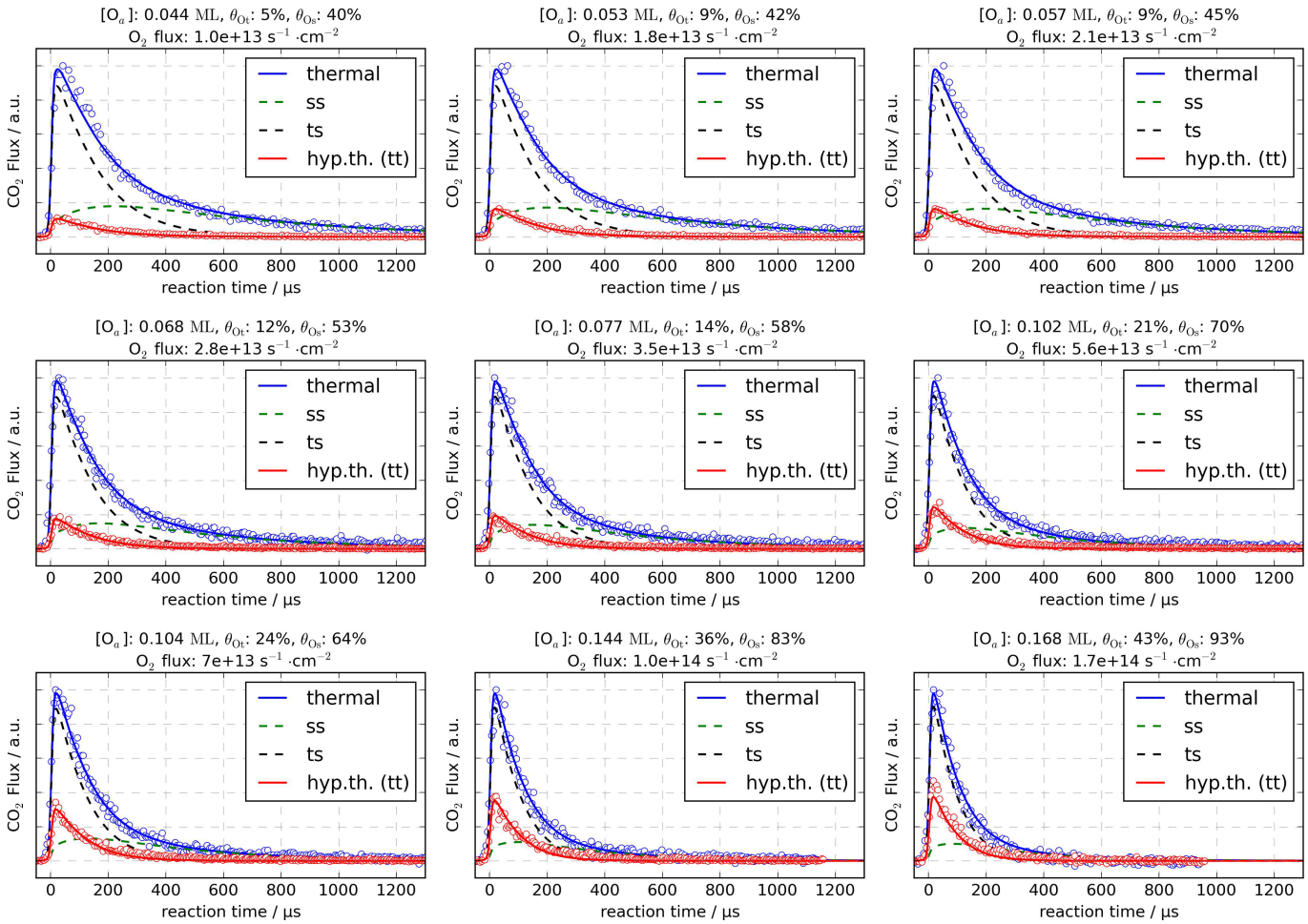

Extended Data Fig. 8 | Examples of the kinetic model fit to experimentally derived kinetic traces for Pt(332). All three reactive contributions are shown. Here $T_S = 320\,°C$ and the oxygen coverage varies from 0.044 to 0.168 monolayers (denoted as [O_a]). The fractional coverage on terraces (θ_{OT}) and steps (θ_{OS}) is also indicated. The time-averaged O_2 flux is stated above each kinetic trace, the time-averaged CO flux was $2.2 \times 10^{12}\ s^{-1}\ cm^{-2}$.

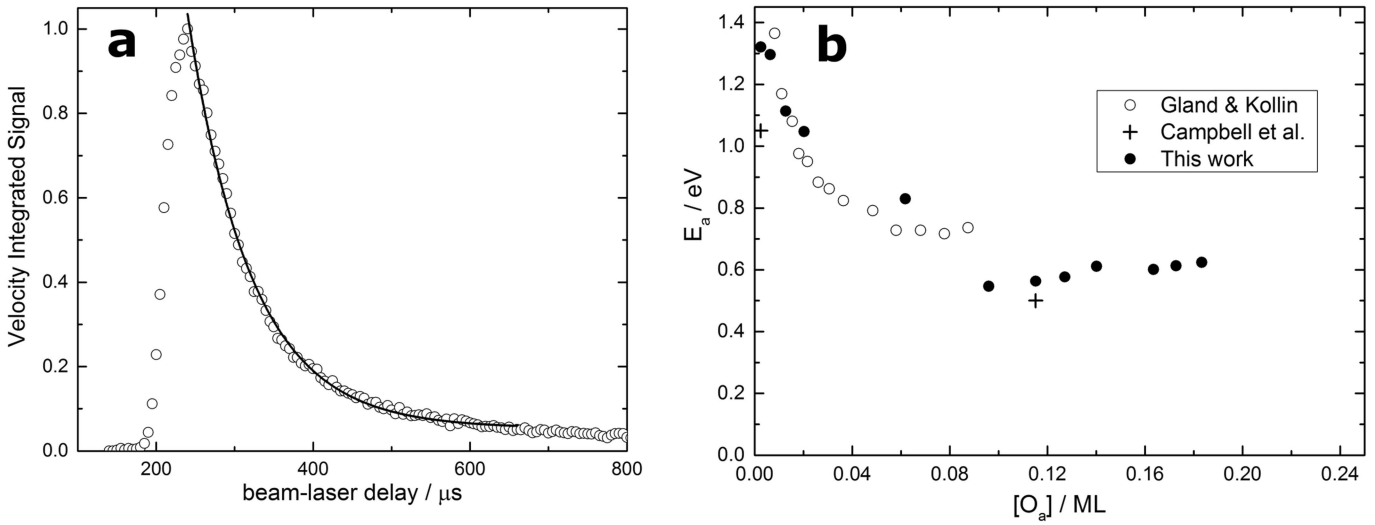

Extended Data Fig. 9 | Activation energies of CO oxidation. **a**, Simulation of previous experiments. We show the kinetic trace integrated over velocity (hollow circles). The solid line shows an exponential fit to the simulated data. **b**, Previously reported activation energies[7,41] (hollow circles) for CO oxidation that were based on product velocity unresolved measurements are compared to the results of this work when integrated over product velocity. See text for details.

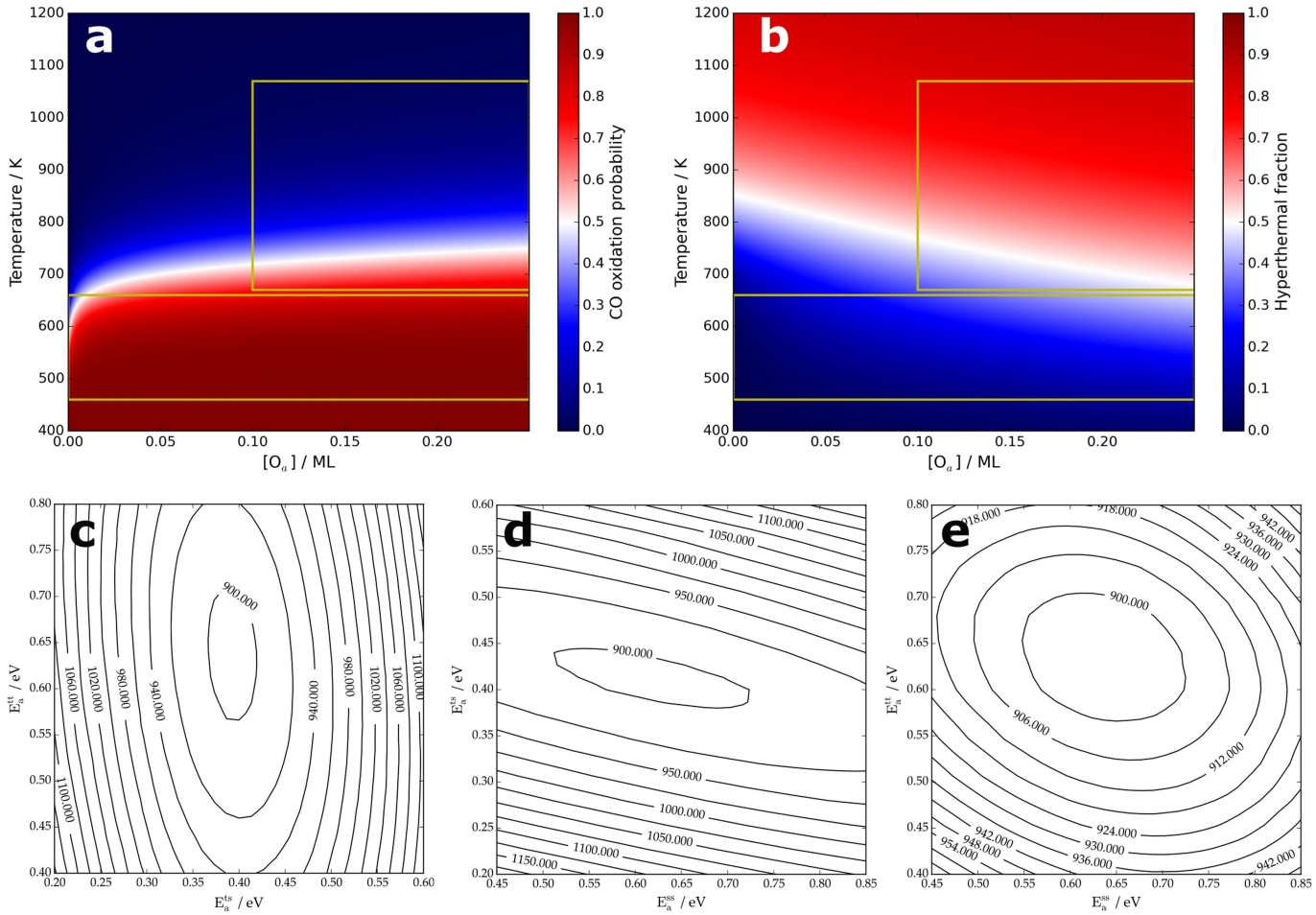

Extended Data Fig. 10 | Model predictions of CO oxidation on a Pt(111) crystal with a step density of 0.25%. a, Total CO–CO_2 conversion efficiency as a function of temperature and oxygen coverage. The yellow boxes indicate (at low temperature) where past studies have been carried out and (at high temperatures) where industrial catalysts are used. **b**, The relative importance of the hyperthermal (terrace) reaction as a function of temperature and oxygen coverage. **c**–**e**, Contour plots showing the total fit residual as a function of two activation energies. *y* against *x*: TT versus TS (**c**), TS versus SS (**d**), TT versus SS (**e**).